PAPER

Thickness dependent tribological and magnetic behavior of two-dimensional cobalt telluride ($CoTe_2$)

To cite this article: Surbhi Slathia *et al* 2024 *2D Mater.* **11** 035006

2D Materials

RECEIVED
13 January 2024

REVISED
29 March 2024

ACCEPTED FOR PUBLICATION
10 April 2024

PUBLISHED
18 April 2024

PAPER

Thickness dependent tribological and magnetic behavior of two-dimensional cobalt telluride ($CoTe_2$)

Surbhi Slathia[1], Cencen Wei[2], Manoj Tripathi[2,*], Raphael Tromer[3], Solomon Demiss Negedu[4], Conor S Boland[2], Suman Sarkar[5], Douglas S Galvao[3,*], Alan Dalton[2,*] and Chandra Sekhar Tiwary[1,6,*]

[1] School of Nano Science and Technology, Indian Institute of Kharagpur, Kharagpur, West Bengal, 721302, India
[2] Department of Physics and Astronomy, University of Sussex, Brighton BN1 9RH, United Kingdom
[3] Applied Physics Department, State University of Campinas, Campinas, SP 13083-970, Brazil
[4] Materials Science and Engineering, Jimma Institute of Technology, Jimma University, Jimma 378, Ethiopia
[5] Materials Engineering, Indian Institute of Technology Jammu, Jammu 181221, India
[6] Metallurgical and Materials Engineering, Indian Institute of Technology Kharagpur, Kharagpur, West Bengal, India
[*] Authors to whom any correspondence should be addressed.

E-mail: m.tripathi@sussex.ac.uk, galvao@ifi.unicamp.br, A.B.Dalton@sussex.ac.uk and chandra.tiwary@metal.iitkgp.ac.in

Keywords: 2D materials, thickness-dependent properties, atomic force microscopy, adhesion, magnetic properties

Supplementary material for this article is available online

Abstract

Two-dimensional (2D) layered transition-metal based tellurides (chalcogens) are known to harness their surface atoms' characteristics to enhance topographical activities for energy conversion, storage, and magnetic applications. The gradual stacking of each sheet alters the surface atoms' subtle features such as lattice expansion, leading to several phenomena and rendering tunable properties. Here, we have evaluated thickness-dependent mechanical properties (nanoscale mechanics, tribology, potential surface distributions, interfacial interaction) of 2D $CoTe_2$ sheets and magnetic behavior using surface probe techniques. The experimental observations are further supported and explained with theoretical investigations: density functional theory and molecular dynamics. The variation in properties observed in theoretical investigations unleashes the crucial role of crystal planes of the $CoTe_2$. The presented results are beneficial in expanding the use of the 2D telluride family in flexible electronics, piezo sensors, tribo-generators, and next-generation memory devices.

1. Introduction

Transition metal dichalcogenides (TMDs) have drawn significant research interest among the family of two-dimensional (2D) materials due to their layer-dependent properties [1]. The origin of these characteristics is due to their honeycomb structure with a unique symmetry and higher surface-to-volume ratio. One of the intriguing features of TMDs, which makes them exceptional, is their tunable bandgap, which varies as the number of layers changes from indirect at multilayer to direct at single layer [2, 3], making them potential candidates for a wide range of electronics, optoelectronics, energy storage, and catalytic applications [4–6]. Therefore, the investigation of the thickness-dependent properties of emerging TMDs have been receiving increased attention in recent years. Cao *et al* revealed that the fracture strength of graphene paper could be improved by decreasing its thickness [7]. Enhancement in film resistivity of WS_2 was observed with decreasing thickness by Romanov *et al* [8]. The strong dependence on the layer number of $NbSe_2$ sheets was observed in their superconductivity transition temperature values [9]. In the field of nanoscale lubrication, there is clear evidence for the role of thickness over a variety of 2D materials for altering the friction force values [10]. The TMDs ($NbTe_2$, VTe_2, Cr_2S_3, etc) are experimentally proven to exhibit magnetic behavior when the layer thickness is decreased [11–13]. However, only a few TMDs have been explored experimentally on the nanoscale, as well-controlled layer thickness up to monolayer is preferable to study the layer-dependent properties of these materials.

Among various TMDs, ditelluride transition metals are gaining attention due to their metallic characteristics in contrast to other related structures, such as selenides and sulfides [14]. Also, tellurides

exhibit unique bandgap sensitivity at lower dimensions under applied strain conditions [15–17]. 2D $CoTe_2$ is a layered material having a hexagonal structure wherein six Te atoms surround one Co atom. Several reports have experimentally proven that $CoTe_x$, in the composition range of $x = 1.3$ up to 2 is metallic due to the decrease in the emission at the Fermi level with the Te content [18]. Recent studies on $CoTe_2$ nanosheets reported that they have good electrical conductivities up to 4.0×10^5 S m^{-1}, with high breakdown current densities up to 2.1×10^7 A cm^{-2} [19], and linear magnetoresistance up to 9 T [20]. Negedu *et al* reported that $CoTe_2$ could behave as a piezoelectric material, and applying small forces (up to 1 N) can result in 5 V of output voltage. They further used 2D $CoTe_2$ to fabricate piezo and triboelectric nanogenerators, which showed excellent high-temperature stability and gave out an output voltage of about 10 V [21]. At the atomic and nano scales, atomic force microscopy (AFM) submodes provide the opportunity to correlate morphology and structure with mechanical, electrical and magnetic characteristics. Significant advances in the study of 2D materials have been made recently owing to developments in AFM-based characterization techniques [22]. In this regard, a variety of suspended graphene membranes' nanomechanical characteristics were mapped by Clark *et al.* It has been found that the force–displacement behavior of monolayer graphene was similar to that obtained with conventional nanoindentation [23]. Additionally, during the fabrication of 2D materials like graphene and MoS_2, the impact of structural defects on strain, doping, and mechanical stiffness was investigated [24]. SPM (scanning probe microscopy)-based local deformation tests were adopted by Susarla *et al* to identify strain-induced ripples at the scratched edges of WS_2/MoS_2 heterostructures, showing a significant interlayer coupling [25]. Oligoglycline tectomer functionalized probe were employed to examine the interfacial interactions between biomolecules and 2D materials. The investigation focused on the tectomer's varying susceptibilities to modify the characteristics of graphene and single- and multilayer MoS_2 [26]. Hence, it would be interesting to comprehensively investigate the nanoscopic size and thickness-dependent $CoTe_2$ properties using different SPM techniques, and it is one of the objectives of the present study.

In the present work, the synthesis of 2D $CoTe_2$ was carried out using the liquid phase exfoliation (LPE) method through simple sonication for layer-by-layer exfoliation from the bulk $CoTe_2$. It is prepared from vacuum induction melting as it is a scalable technique and produces good quality (crystalline with a small number of impurities) nanomaterials at a reasonable cost [27]. X-ray diffraction (XRD) technique and microscopy images confirmed the formation of 2D layered $CoTe_2$ nanoflakes. The produced 2D $CoTe_2$ was extensively investigated through atomically resolved transmission electron microscopy to determine the lattice spacing as a function of the number of layers. The samples were further investigated through nano mechanics (mechanical mapping), tribo-mechanics (lateral force microscopy (LFM)), surface potential distribution (Kelvin probe force microscopy (KPFM)) and nanoscale magnetism. We also carried out fully atomistic computer (density functional theory (DFT) and *ab initio* molecular dynamics (AIMD)) simulations to better interpret the experimental data and associated physicochemical mechanisms. The obtained results add important information on the emerging class of tellurides and their use in applications for next-generation electronic devices.

2. Materials and methods

2.1. Experimental details

Bulk $CoTe_2$ was prepared with vacuum induction melting method by using cobalt and tellurium (99.99% purity) in a stoichiometric ratio of 17.5 wt% of cobalt and 82.5 wt% of tellurium for the composite formation. The alloy was made by melting the elements in a quartz tube at a temperature of 1050°C in a melting chamber under an argon atmosphere. The melting chamber was kept at a high vacuum condition of 10^{-5} mbar for obtaining pure alloy and preventing oxidation. Then, the prepared composite was furnace cooled and converted to powder using mortar and pestle. From these powdered bulk samples, 2D $CoTe_2$ samples were prepared by taking 50 mg of the bulk sample in 150 ml of isopropyl alcohol and ultrasonicated in a probe sonicator ($f = 30$ kHz) for 5 h at room temperature to obtain exfoliated $CoTe_2$ sheets. The 2D $CoTe_2$ powdered sample was mixed into 10 ml of IPA and ultrasonicated for up to 30 minutes. The dispersion was spin-coated over the Si wafer at 1000 rpm for 1 minute. The prepared sample was further used for the doing AFM analyses.

The diffraction patterns and crystalline phase information of the sample were taken from Bruker, D8 Advance XRD with Cu-$k\alpha$ radiation having 1.5406 Å wavelength (λ) with 40 kV voltage and 40 mA current as operating conditions. WiTec UHTS Raman spectrometer 300 VIS, Germany, having an excitation wavelength of 532 nm was used for Raman spectrum analysis at room temperature. To study the surface composition and oxidation states of exfoliated $CoTe_2$, the PHI 5000 Versa probe-III scanning XPS (x-ray photoelectron spectroscopy) microprobe was used. To study topographical, compositional, and crystalline properties FEI, Themis 60–300, and FEI-Ceta 4k × 4k camera high-resolution transmission electron microscopy (HRTEM) were used.

AFM was used for nanoscale imaging, potential mapping, lateral force microscopy (LFM) and magnetic force microscopy (MFM). All these characteriz-

ations were carried out using the Bruker Dimension Icon instrument at room temperature with 35% relative humidity. The AFM was positioned in the insulated box over an anti-vibrant stage to mitigate the environmental noise and building vibrations. For each mode, specific cantilevers were used for measurements as follows:

AFM was carried out with quantitative nanomechanical mapping mode, 'an areal collection of force–displacement spectroscopy' for measuring the variation in mechanical properties such as modulus, adhesion, and indentation along the thickness changing from monolayer to bulk. For the measurements, probe stiffness, driving frequency, and tip radii were taken at values of 5 ± 0.5 N m^{-1}, 150 kHz, and 10 ± 2 nm, respectively. For calibration of the cantilever, Sader's method [28], as well as thermal tuning, were used. The uniqueness of peak force (PF)-AFM in tapping mode is that the maximum normal force applied at each point on the sample surface can be controlled using a feedback system that keeps the maximum force constant while scanning. Silicon nitride probes and Sn doped Si probe (Model: RTESPA-150, Bruker) with stiffness and drive frequency of 5 ± 0.5 N m^{-1} and 150 kHz approximately, and tip radii of 10 ± 2 nm were used for the measurement. LFM: to measure the lateral force by sliding the tip apex in trace and retrace direction a silicon cantilever of stiffness 0.4 N m^{-1} (Model: CSG10, NT-MDT) was used. KPFM: PF-Kelvin probe microscopy (Model: PFQNE-AL) to measure contact potential difference (CPD, volts). MFM: Bruker MESP probes (cobalt–chromium coating on tip apex) have been used for the investigation. The influence of the localized magnetic field has been measured through phase image in interleave mode.

2.2. Theoretical detail

In order to obtain further insights and to better interpret the experimental results, we carried out *ab initio* calculations at the DFT level. We use the cut-off energy of 250 Ry and *k*-points mesh of 2 × 2 × 2 within the local density approximation functional and Ceperley and Alder parametrization [29] and single zeta basis. We assume that when forces in each atom are less than 0.05 eV $Å^{-1}$, the convergence criteria to the optimization process were achieved. All calculations were performed with SIESTA software [30].

We considered, in our theoretical analyses, structural models to mimic the experimental conditions, i.e. the $CoTe_2$ layers were deposited on silicon oxide (silica, SiO_2). We deposited at the substrate slab fragments of 2D $CoTe_2$ corresponding to from one up to four layers at three different crystallographic orientations: [001], [010], and [001]. The heterolayer structures are then fully geometrically optimized.

Once we obtained these optimized structures, we carried out two types of analyses: (i) the energy layer adhesion, and; (ii) a Tip indentation on the 2D $CoTe_2$ layers. The Tip was modeled using a triangular Si_3N_4: shaped/pyramid, which is the same tip material used in the AFM measurements. The adhesion of layers was calculated considering the work necessary to extract each layer from different sizes, using the expression (1) [31]:

$$W_{\mathrm{ad}} = \frac{E_{\mathrm{SiO_2}} + E_{\mathrm{2DCoTe_2}} - E_{\frac{\mathrm{2DCoTe_2}}{\mathrm{SiO_2}}}}{A} \tag{1}$$

where $E_{SiO2} + E_{2DCoTe2}$ are total energy values for the isolated SiO_2 and 2D $CoTe_2$, respectively, $E_{2DCoTe2/SiO2}$ is the total energy value for the 2D heterostructure $CoTe_2/SiO_2$, and A is the contact area between them. From equation (1), we calculated the work of adhesion (W_{ad}) for different separation values of sample and substrate. The W_{ad} values were estimated from the universal binding energy relation curves [31], which is a fitting process to calculate the work of adhesion as a function of 2D $CoTe_2$ number layers and their separation distance from the silica substrate.

For the analysis of Si_3N_4 Tip penetration on the 2D $CoTe_2/SiO_2$ heterostructure, we performed AIMD simulations with an NVT ensemble and integration time of dt = 1.0 fs. We simulated the Tip processes assuming indentation step movements of 0.5 Å, in which, for each step, an AIMD run of 0.5 ps is performed. When the Si_3N_4 Tip penetrates the $CoTe_2$, it produces a compressive stress (negative value) along the Z direction. It relates to the force through the expression:

$$S_z = -\frac{F}{A} \tag{2}$$

where S_Z is the stress component along the Z direction, F is the force applied to the system, and A is the contact area at which the force is applied.

3. Results and discussion

The schematic representation of the formation of layered 2D $CoTe_2$ from its bulk counterpart is described in figure 1(a) where probe sonication has been used to carry out LPE. The crystalline arrangement was investigated through XRD patterns for both bulk and exfoliated 2D $CoTe_2$, shown in figure 1(b), indexed to non-centrosymmetric space group Pnn2 (No. 34) with lattice parameters of a = 5.329 Å, b = 6.322 Å, and c = 3.908 Å. An intensity difference was observed due to the exfoliation of $CoTe_2$ into preferential planes. The peaks were observed at 28.3°, 31.7°, 32.9°, 47.2°, 54.31°, and 58.2°, in exfoliated $CoTe_2$, which are characteristic peaks of orthorhombic crystalline structures. HRTEM images of the polycrystalline telluride flakes

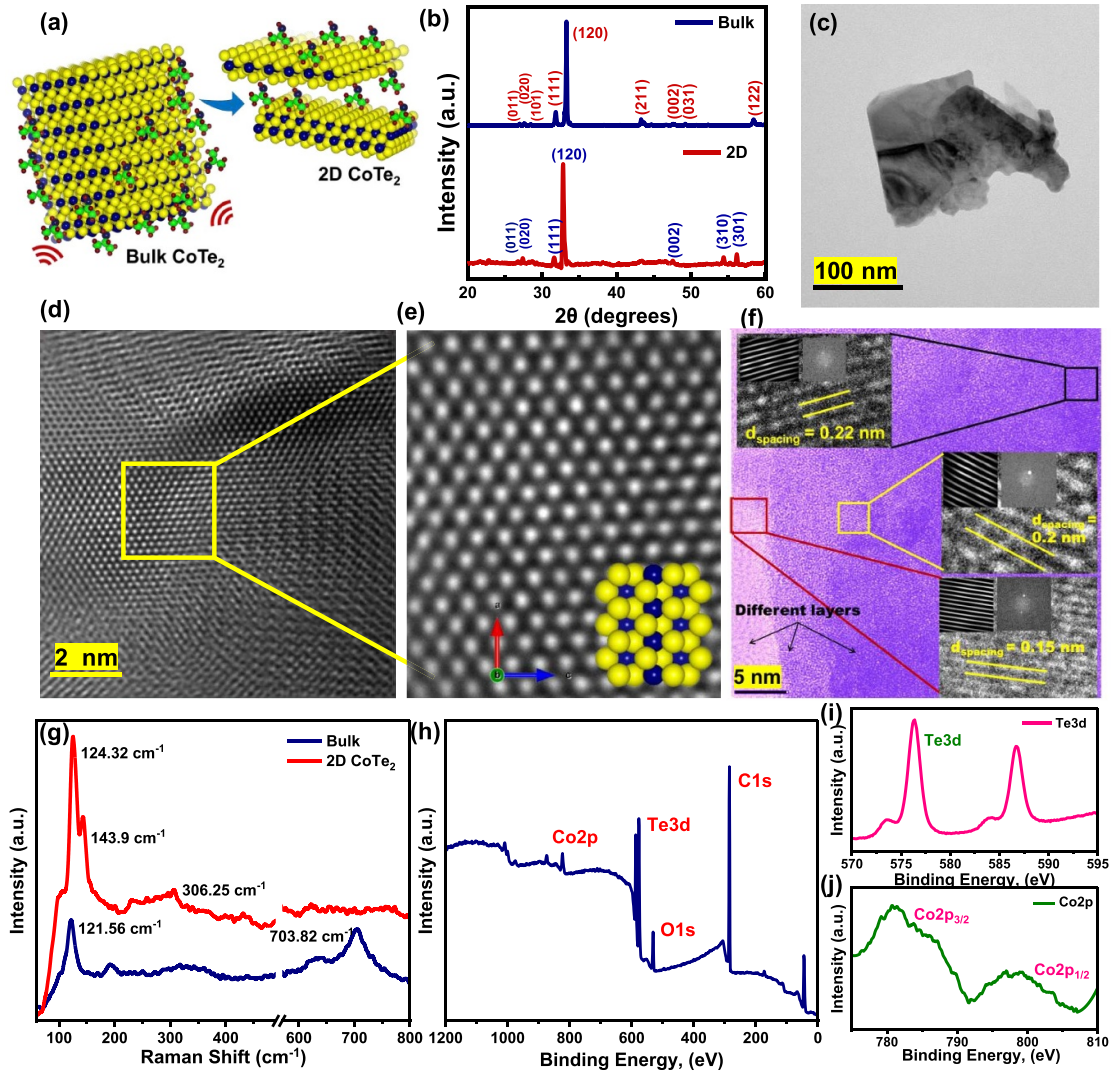

Figure 1. Structural and morphological characterization of 2D $CoTe_2$. (a) Schematic representation of synthesis procedures of 2D $CoTe_2$, (b) x-ray diffraction pattern of bulk and 2D $CoTe_2$, (c) HRTEM image of a $CoTe_2$ flake, (d) Different crystallographic orientations observed in the HRTEM image, (e) Magnified image distinguishing Co and Te atoms and (f) TEM image showing different layers of 2D $CoTe_2$ nanoflake (magnified view of different crystal plane orientations, the insets show FFT and inverse FFT analyses), (g) Raman spectra of bulk and 2D $CoTe_2$, (h) XPS spectra of 2D $CoTe_2$, (i), and (j) Te3d and Co2p XPS spectra, respectively.

of different thicknesses are presented in figure 1(c). The atomic resolution identifies different crystallographic plane orientations (figure 1(d)) with different atomic arrangements. A zoom-in region of a particular plane in figure 1(e) confirms the presence of two types of atoms: Co and Te, which are depicted by white and black color balls, respectively. The Co atomic number is smaller than Te's, thus, it shows a weaker contrast compared to Te. The arrangement of Co and Te are shown using blue and yellow colors, respectively (figure 1(e)), revealing the $CoTe_2$ hexagonal structure. The distinction between the $CoTe_2$ structures with a different number of layers (consequently, having different contrasts) can be clearly seen in figure 1(f). The insets show the FFT (fast fourier transform) and inverse FFT analysis of the plane orientation observed in these different layers. The $d_{spacing}$ was calculated for the different layers of the $CoTe_2$ nanoflake, indicating a gradual increase with thin layers having $d_{spacing}$ value of approximately 0.15 nm and thick layers having 0.22 nm. This plays a crucial role in influencing the mechanical properties, surface chemistry, surface potential, and magnetic properties as discussed in the subsequent sections.

The Raman spectra of bulk and 2D $CoTe_2$ is as shown in figure 1(g). The prominent peaks were obtained at 124.32, 143.9 and 306.25 cm^{-1} for the exfoliated sample. The A^1 mode at 124.32 cm^{-1} can be attributed to the movement of atoms in the basal plane found in most of the tellurides [32]. The E^2 mode at 143.9 cm^{-1} is associated with asymmetric stretching predominantly along the

c-axis [33]. Compared to the 2D $CoTe_2$, an additional peak observed at 703.82 cm^{-1} in the case of bulk was assigned to the stretching mode of the TeO_3 trigonal pyramid units [34]. The XPS spectra of the samples are shown in figure 1(h) with the presence of the characteristic peaks of cobalt, tellurium, oxygen and carbon. Figure 1(i) shows the core level region of Te 3d having peaks at 576 eV and 587 eV, which corresponds to the Te^{4+} state i.e. Te $3d_{5/2}$ and Te $3d_{3/2}$, respectively [35]. The other two peaks might be due to surface oxide formation with Co while exfoliating. Figure 1(j) shows the deconvoluted peaks of 2D $CoTe_2$ where the peaks at about 780 eV and 798 eV are mainly due to Co $2p_{3/2}$ core level and Co $2p_{1/2}$ spin–orbit coupling, respectively [36].

The morphology of the 2D $CoTe_2$ flakes of different thicknesses and their corresponding mechanical response against calibrated tip apex was investigated through AFM; see experimental section for calibration of cantilevers. The nanoscale mapping through PF tapping probe microscopy (PF-AFM) is useful to obtain the mechanical properties of the telluride sheets under elastic conditions (i.e. without damage) of varying thickness from 1 up to 9 nm, figures 2(a) and (c). Thus, the concurrent maps of modulus, adhesion force, and indentation depth were obtained in a single acquisition for a valid comparison, assuming unaffected tip radii [37]. The Derjaguin–Muller–Toporov (DMT) [38] contact mechanical model was used, as it is applicable for stiff samples having low surface energies and includes van der Waals forces outside the contact region. As per this model, the tip–sample surface interaction force under the influence of adhesion force can be given by the relation (3):

$$F = \frac{4}{3} E^* \sqrt{R(d - d_o)^3} + F_{\text{adhesion}} \qquad (3)$$

where R is the tip radius, d_o is the surface rest position, ($d - d_o = \delta$ (nm)) is the sample deformation under tip indentation depth. E^* is referred as effective elastic modulus of tip and sample, and F_{adhesion} is the adhesion force during contact. The contact mechanics in the DMT conditions is useful to obtain the mechanical properties over various thickness of 2D $CoTe_2$ shown in figures 2(c) and (d). The retraction force–displacement curves for 2D $CoTe_2$ nanoflakes from monolayer to bulk are illustrated in figure 2(b). From these retraction force calculations, we observed a gradual reduction in the adhesion force 'pull-out'. Figures 2(e)–(g) summarizes the trend of average values of adhesion force (nN), modulus (GPa), and indentation depth (nm) values from several telluride sheets showing decreasing adhesion force, modulus, and increasing indentation depth at fixed normal force value. The adhesion force values depend on two major factors: the interfacial contact area between the tip apex-topmost layer of the 2D material under deformation and the interfacial interaction through static electric charges.

The indentation depth (δ) represents the vertical separation between jump-to-contact and maximum force point in the approach curve of the force–distance spectroscopy (see supplementary information (SI) figure S6) [39]. The increment of indentation depth (nm) indicates the higher contact area with increasing thickness (figure 2(g)) results in higher adhesion force as observed in graphene (see inset figure 2(e)). Nevertheless, the lowering of adhesion force in the telluride sheets confirms the predominance of the static interfacial charges for determining the interfacial interaction (i.e. the metallic tip experiences a repulsion force from the thicker telluride sheets). Further, the increment of the indentation depth also explains the softness (1*l*: 1.4 ± 0.5 GPa, 2*l*: 0.8 ± 0.5 GPa and bulk: 0.6 ± 0.5 GPa) with increasing thickness, similar to the graphene sheets (see the inset of figure 2(f)) of varying Young's modulus from 2.4 TPa to 1 TPa from monolayer to bulk [40, 41]. The additional factor responsible for mechanical characteristics with thickness is increasing the lattice constant, which leads to weak binding between metal and chalcogenides. During indentation, the interlayer stacking error, i.e. interlayer sliding in multilayer 2D materials, can also be a factor for the decrease in modulus values with increasing thickness [42]. Thus, 2D $CoTe_2$ sheets share a similar mechanical response with graphene layers with distinct interfacial interaction that will be discussed through the surface potential map by KPFM in the subsequent section. One of the advantages of having low adhesion forces is the potential use of the 2D $CoTe_2$ sheets as a solid-state lubricant and tribo-generators [21]. The friction map generated from shear forces between the sliding tip and the telluride sheets shows lower resistance to sliding/delamination, figure 2(h) (inset concurrent friction map). The average values of friction force (nN) decrease with thickness, as shown in figure 2(i). This tribological trend is in good agreement with the pioneer works of Lee *et al* [10] and Filleter *et al* [43], addressing the frictional behavior of 2D materials for different thicknesses. This trend is observed (although with different frictional values) for the majority of 2D materials, including graphene and MoS_2 [44–46]; see inset figure 2(h). It has been proposed that thin layers of a 2D material with weak interlayer and substrate interactions are susceptible to deform out-off plane ('a puckering effect') under shear forces, as depicted in schematic figure (S2) in the SI. When the AFM tip slides over the surface of the sample with a finite normal force, a puckered structure (i.e. temporary wrinkle-like topology) is formed around the tip, which increases the contact area and thus induces higher friction. However, as the number of layer increases, the bending rigidity increases

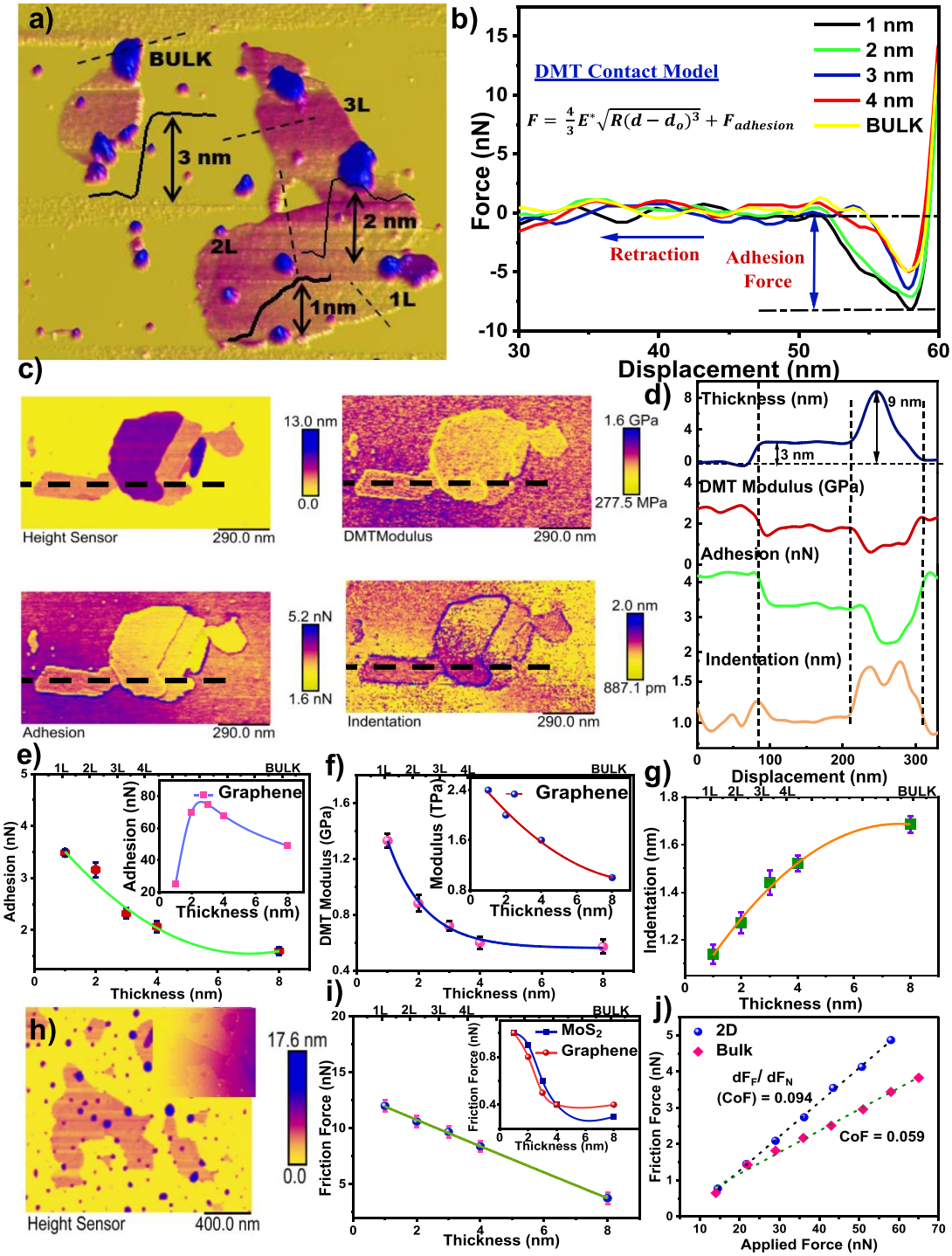

Figure 2. The concurrent surface chemistry (adhesion force) and mechanical response (DMT modulus, indentation map) from $CoTe_2$ sheets. (a) AFM topography of 2D $CoTe_2$ layers distributed from monolayer to bulk at different locations, (b) The force–displacement retraction curves from a few layers to bulk show an adhesion force (pull-out) from different thicknesses. The inset presents the contact-mechanical model used to measure the mechanical properties under the influence of the adhesion forces, (c), (d) Topographical images and corresponding line profile of 2D $CoTe_2$. The dashed line shows the thickness of an individual sheet and its mechanical response toward the AFM tip apex sheet quantified through the line profile. (e)–(g) Variation in average values of adhesion, modulus, and indentation as a function of the thickness. The insets show a comparison with graphene [40, 47]. (h), (i) Frictional map and its characteristics at different thicknesses compared to other 2D materials (inset [45]), and (j) Calculation of the friction coefficient from the applied force Vs. friction force graph of a fixed thickness.

along the vertical direction, suppressing the puckering and consequently lowering the friction force. A generalized form of nanoscale frictional feature can be described through the coefficient of friction values through a first derivative of load-dependent friction (figure 2(j)). The estimated value of 0.094 brings tellurides close to the category of graphene and MoS_2 as good solid-state lubricants.

DFT and AIMD simulations were carried out using structural models to mimic the experimental

conditions of the contact interaction of the 2D $CoTe_2$ layers with a SiO_2 (silica) substrate. We used a Si_3N_4 shaped/pyramid tip (the same tip material used in the AFM measurements) to simulate the indentation processes. The adhesion energy variations and the structural distortions of the 2D layers during the simulated indentations. See the experimental section for details. The adhesion energy (J m^{-2}) is measured as a function of the separation distance (Å) between the telluride sheet/s (1*l* and 2*l*) against the SiO_2 surface (see figures 3(a) for the telluride crystal plane [010]). The optimized structures showed that the charge in the SiO_2 substrate remains practically the same, and no significant charge transfer has been observed from $CoTe_2$ to the SiO_2 substrate. A slight decrease in the adhesion energy value from 1*l* (1.7 J m^{-2}) to 2*l* (1.66 J m^{-2}) corroborates the trend observed from force–distance spectroscopy measurements. The in-depth analysis indicates that negative static charges on the interface of $CoTe_2/SiO_2$ (26 me) decrease as a function of the number of layers that play a crucial role in determining the adhesion energy value. It is important to remark that this trend of adhesion energies has been observed for other crystal planes [100] and [001], see SI (figure S5), which suggests that the above-mentioned trend is crystal-oriented dependent and consistent with the different static charges' values 126 and 35 meV along [100] and [001] plane respectively. Also, we considered our structures in vacuum and defectless, while the experiments were in an ambient environment (35% of relative humidity) and comprised structural defects, as evidenced by the microscopy results. Broadly, the adhesion energy of $CoTe_2$–SiO_2 depends on the crystal plane interfacing the silica substrate, and lies in the range of 0.97–1.70 J m^{-2}, which is similar to other 2D materials, such as 1*l* graphene–SiO_2 (0.72 J m^{-2}) [48], MoS_2–SiO_2 (0.17 J m^{-2}) [49]. Graphene has shown a parabolic trend in the adhesion energy from 1*l* to 3*l* (2*l*: 1.4 J m^{-2} and 3*l*: 1.3 J m^{-2}), indicating saturation of one type of charge at the bilayer [50].

We also estimated Young's modulus (Y_M) values from the DFT simulations. The procedure is to introduce small strain values (∼1%) along the *X* and *Y* directions separately and then obtain the Y_M values from the slope of the stress versus strain curves. The Y_M values for different crystallographic directions as a function of the number of layers are presented in figure 3(b). It is observed that the different crystallographic directions do not show the same trends. The obtained numbers are consistent with the corresponding experimental ones. The simulated indentation procedures were performed through AIMD simulations. We considered a rigid indenter (Si_3N_4) that is moved (perpendicularly) toward the $CoTe_2/SiO_2$ structure up to a penetration depth of 0.5 Å, as schematically shown in figure 3(c) for the case of $CoTe_2$ [100] plane. The corresponding AIMD snapshots at different time frames (fs) show a gradual penetration of the indenter and accumulation/dissipation of induced stress through each layer to the silica substrate, which is different for each crystallographic direction. The corresponding results for the [010] and [001] directions are presented in the SI based on the atomic charge distribution. [100] undergoes a minor deformation (up to the depth of 3.5 Å) due to an efficient stress transfer to the silica substrate (silica amortization). Figure 3(d) presents the force as a function of the depth values. We can see from this figure that the general trend is that the force decreases as the depth value increases. The same behavior was observed for the other crystallographic directions (results presented in the SI). Although the values from the simulations are larger than those experimentally obtained (expected as the simulations considered pristine defect less structures), the qualitative behavior is the same experimentally observed and further validates the thickness softness effect.

As discussed above, the thickness dependence of 2D $CoTe_2$ sheets influences their mechanical properties and interfacial adhesion energy. Its critical effect also applies to surface electric potentials and localized magnetic fields, sensed by separate functionalized probes of metallic and magnetized coating (cobalt–chromium) coatings, respectively. The CPD (volts) observed during PF-KPFM measurements shows topography (figure 4(a)) corresponding to surface potential distribution of different thicknesses, figures 4(b) and (c). The average values of work function (eV) were calculated from surface potential values using an expression (SI equation (4)) showing a decreasing trend with thickness, inset of figure 4(c). The decreasing values of work function with increasing thickness indicate higher electron concentration at the thick layer. This phenomenon can be explained by electrostatic interlayer screening [51], i.e. charge redistribution among each layer induced from the substrate as observed in graphene by Kim and co-workers [52]. Therefore, increasing the negative charges with the addition of a telluride layer repels the similar negative charges on the sliding probe responsible for the lower adhesion with higher thickness. Nevertheless, interlayer interaction (in a thick sheet) against the tip apex cannot be ignored [53]. One can stimulate the surface with biasing and modulate the static charge interaction, consequently, adhesion force from 2D material for the desired application [26].

The magnetostatic interaction between the stray magnetic field from the $CoTe_2$ and magnetic sensor was investigated as the function of thickness. The magnetized probe (see experimental section) is slid at constant lift height (LH) to detect the force gradient of the stray field. The vertical force gradient from different sheet thicknesses shifts the magnetic sensor resonance frequency (f_o) proportionally. The frequency

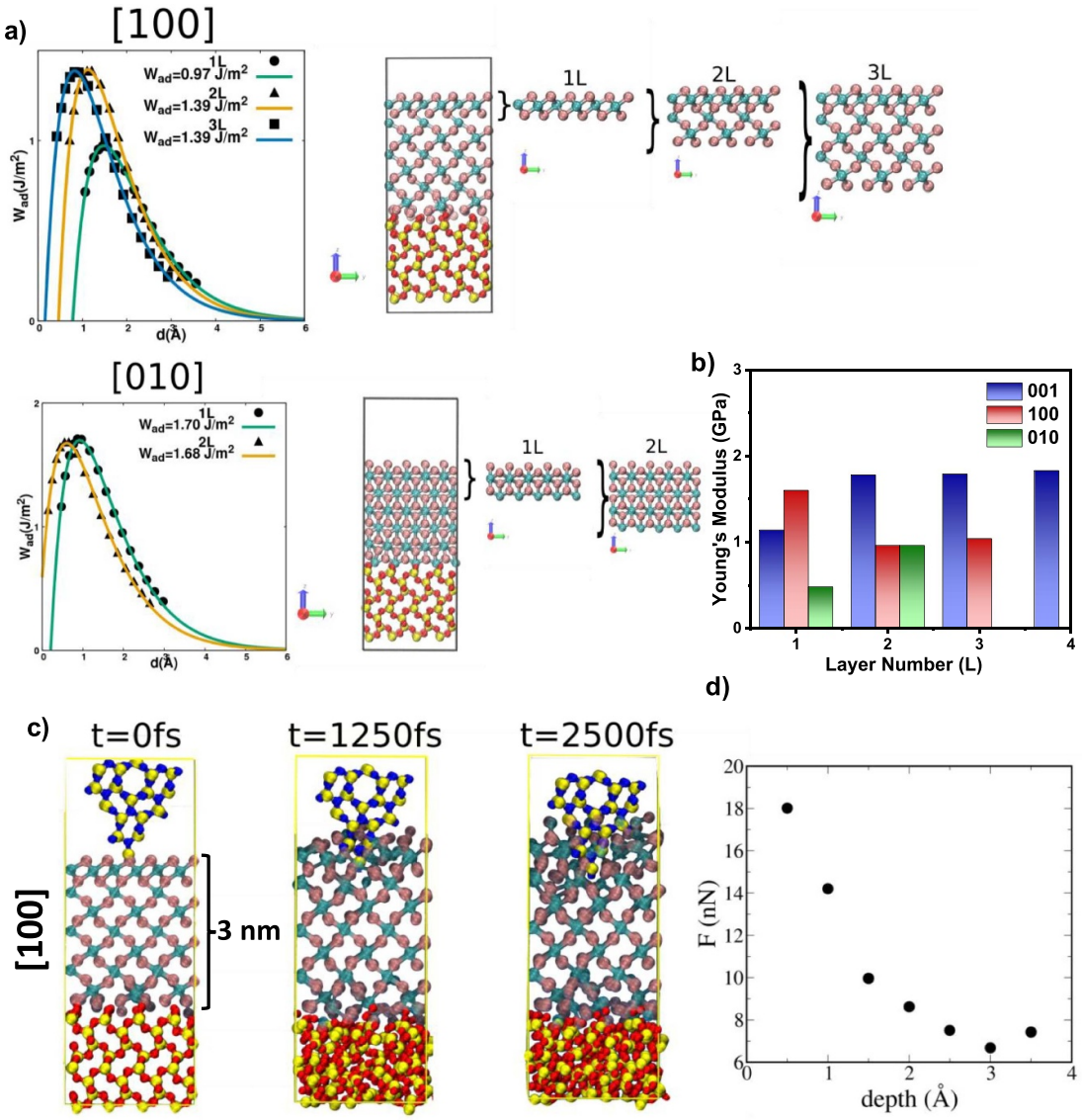

Figure 3. Schematic of structural models (lateral views) of the 2D $CoTe_2/SiO_2$ interfaces (we considered from a single layer (1L) up to four layers (4L)). (a) The adhesion energy values, as a function of the separation distance for the [100] and [010] cases. (b) Young's modulus values as a function of the number of layers for the crystallographic directions considered here. (c) Indentation process of three layers (3L) at different time frames (0 fs, 1750 fs and 3500 fs) from the event of 'jump-to-contact' to a finite indentation depth. (d) Indentation force (nN) as a function of the depth value (Å).

shift (Δf) is detected through the phase of oscillations. In the present set-up, the cantilever phase signal upper shift indicates the magnetic sensor repulsion from the stray magnetic field and vice-versa for the downshift (see scale bar in figure 4(e)). The phase image reveals that a limited region of the $CoTe_2$ sheet is susceptible to the magnetic field, which is quantified through the phase signal profile. It is observed that thicker $CoTe_2$ (around 7 nm) showed the signature of the magnetic attraction, which was not observed in the thinner sheets of 3 nm (see figures 4(f) and (g)). It is worth mentioning that MFM technique is well suited for highly magnetized samples, nevertheless ineffective toward weak stray fields generated from subtle magnetic regions [54]. DFT simulations were also carried out to investigate sub-nanoscale magnetic properties of 2D $CoTe_2$ through the calculation of collinear spin polarization (see SI, figure (S5) for details). It was observed that magnetic moment (μ) increased with thickness for the crystal direction [100], as follows: ($\mu_{1L} = 0.43\ \mu_B$, $\mu_{2L} = 0.56\ \mu_B$, and $\mu_{3L} = 0.58\ \mu_B$). For the other crystal planes ([010], and [001]), different trends were observed ($\mu_{1L} = 0.62\ \mu_B$, and $\mu_{2L} = 0.57\ \mu_B$), ($\mu_{1L} = 0.77\ \mu_B$, $\mu_{2L} = 0.62\ \mu_B$, $\mu_{3L} = 0.57\ \mu_B$), respectively, where, μ_B is the Bohr magneton constant. The DFT results also indicate that the magnetization of $CoTe_2$ is direction-dependent, it increases for [100], and decreases to [010] and [001].

Since the magnetic contrast in MFM is highly dependent on the LH, we carried out MFM measurements at various LHs to investigate the magnetic

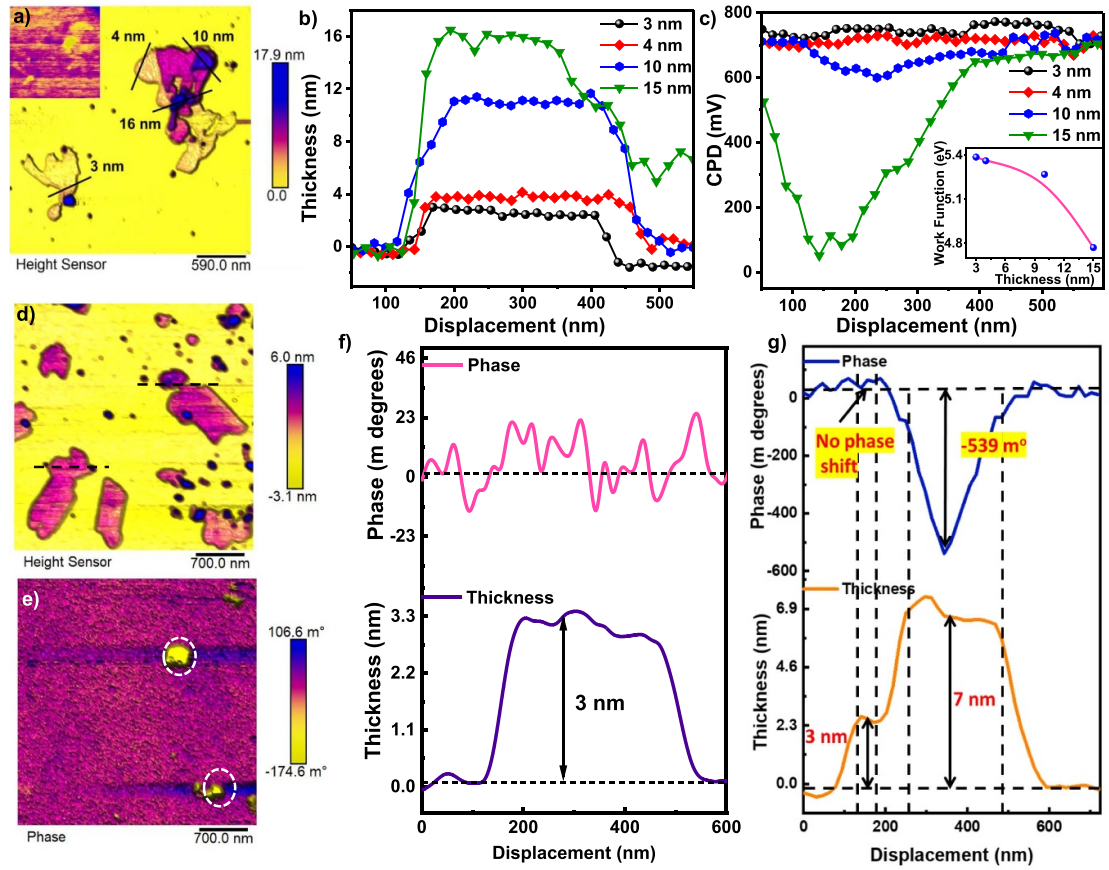

Figure 4. Work function and MFM measurements of $CoTe_2$ sheets. (a) Topographical image of $CoTe_2$ nanoflakes, (b) variation in thickness vs displacement plot, (c) change in CPD (mV) with respect to the different thicknesses with the inset showing the work function values as a function of the number of layers, (d) AFM topography of $CoTe_2$ sheets obtained using a magnetic sensor, (e) phase image susceptible to the stray magnetic field at the lift height of 20 nm of the same region illustrates selected regions (marked by dashed circles) in the $CoTe_2$ sheet. (f) line profile over $CoTe_2$ sheet of 3 nm height showing no influence from the stray magnetic field in the phase signal, and (g) line profile from the 7 nm thick sheet and its concurrent phase profile revealing significant phase shift from the region of $CoTe_2$.

properties of 2D $CoTe_2$ with different thicknesses. Through MFM, concurrent height profile information and interleave phase signal have been observed. The phase response is a consequence of the interaction between the magnetized AFM probe's field and the magnetic domains (parallel and antiparallel) from the sample operated at vertical separations (so-called LHs). Thus, different LHs reveal valuable information about the gradient of stray magnetic fields from 2D $CoTe_2$, as shown in figure 5(a). The MFM images exhibit resolution details of the surface magnetic domains at the LHs from 20 nm to 25 nm and decrease after 35 nm for all thicknesses. The corresponding plot profiles at different LHs, as shown in figure 5(b), align with the morphology of the 2D $CoTe_2$. A distinguishable magnetic characteristic has been observed between 3 and 6 nm thickness 2D $CoTe_2$ for LHs of 20 nm and 25 nm. The negative phase shift reflects the attractive interaction between the probe and the sample, found higher in the 6 nm thickness sample. This is because, under the attractive magnetic field interaction, the resonance frequency ($\omega_o \approx 73.43$ KHz) of the cantilever decreases, resulting in negative phase shift change (Δ phase^o). Lowering of LH further increases the Δ phase^o, indicating a higher magnetic moment of the thicker layer than thin 2D $CoTe_2$. It is suggested that nominal positive values of Δ phase^o imply lesser magnetic response or the dominance of electrostatic repulsion [55, 56].

Interlayer interactions between the telluride sheets and the cumulative spin moments can explain the overall magnetic properties of 2D lamellar $CoTe_2$. It has been found in previous studies that the magnetic behavior of the different layers depends on the stacking sequence of the crystal. Since the interlayer van der Waals bonding is weak, this can result in different stacking polytypes. For instance, Li *et al* reported that in the monoclinic stacking sequence of CrI_3, the spin coupled to each other results in an antiferromagnetic behavior, whereas if the layers were arranged in a rhombohedral manner, it resulted in a ferromagnetic interlayer exchange [57]. It is worth noting that the linear growth of magnetic moment

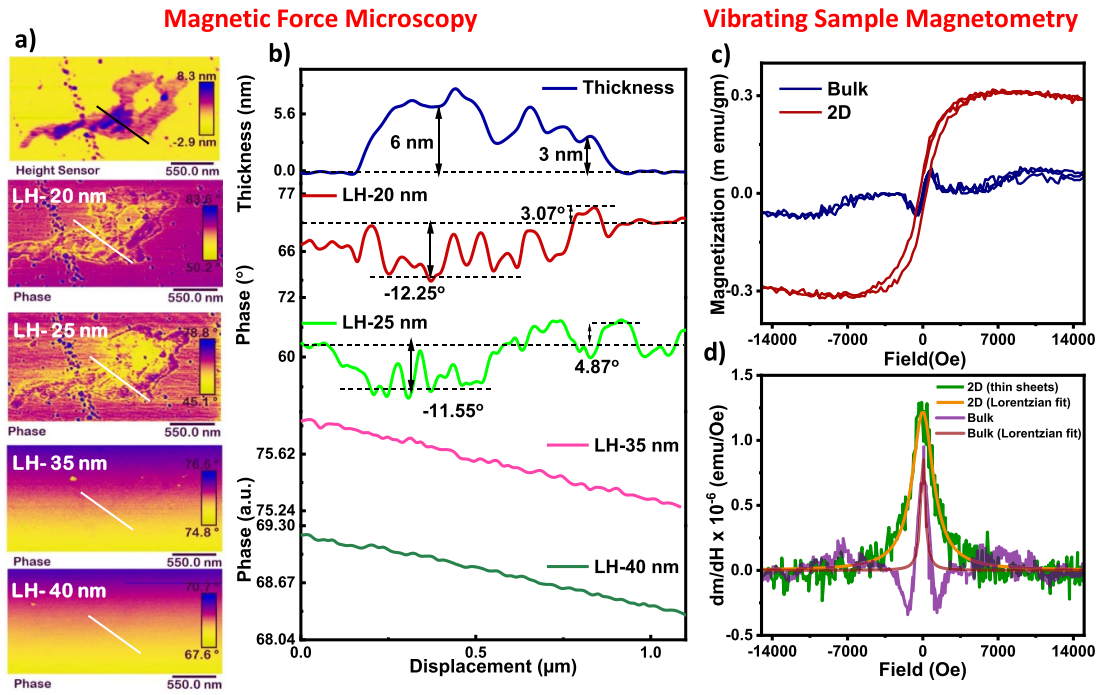

Figure 5. Lift-height based MFM measurements and vibrating sample magnetometry measurements of bulk and exfoliated $CoTe_2$. (a) Topographic images of magnetic force microscopy measurements of exfoliated $CoTe_2$ at different tip lift heights, (b) Phase plot profiles of exfoliated $CoTe_2$ at different lift heights, (c) magnetization vs field graph of bulk and exfoliated $CoTe_2$, and (d) dm/dH (emu Oe^{-1}) vs field (Oe) comparative study of bulk and exfoliated $CoTe_2$.

with increasing thickness is not always obvious, as observed by Li and coworkers for another TMD (MoS_2) [55]. Additional factors, such as variations in the stacking arrangement, presence of defects, vacancies, etc, could also change the cumulative spin moments and influence the lamellar material's magnetic properties [58, 59].

The macroscale magnetic behavior of 2D $CoTe_2$ was investigated through vibrating sample magnetometry performed at room temperature (300 K), as shown in figure 5(c). The magnetic ordering of bulk $CoTe_2$ is weaker as compared to 2D $CoTe_2$. The saturation magnetization in 2D $CoTe_2$ is 0.321 emu gm^{-1}, which is four times larger than the corresponding bulk value (79.61×10^{-3} emu gm^{-1}). The magnetic coercivity (H_c) and retentivity (M_r) for 2D $CoTe_2$ are 311.90 Oe and 384.56×10^{-6} emu, respectively, which are larger than the bulk $CoTe_2$ (43.77 Oe and 118.18×10^{-6} emu). The appearance of a hysteresis loop in the 2D $CoTe_2$ shows the presence of a soft ferromagnetic nature. According to figure 5(d), it is anticipated that the full-width half maximum of the first derivative for 2D $CoTe_2$ has a broader distribution of magnetic moments and hence exhibits better magnetization with respect to a given field than the bulk counterpart, which exhibits a weaker magnetization, as shown in the fitted curve. The previous work on bulk $CoTe_2$ reported its ferromagnetic behavior being suppressed due to strong spin fluctuations, thereby maintaining its paramagnetic nature [60]. The current work is the first paper on magnetic and mechanical properties correlation of 2D $CoTe_2$. In future, a detailed temperature dependent magnetic properties studies can reveal several interesting unexplored physics of the unique $CoTe_2$. However, no experimental validation of changing the magnetic nature to ferromagnetic after exfoliation with varying thicknesses has been reported. Hence, our research sheds light on the intriguing magnetic properties of 2D $CoTe_2$ and opens new perspectives for future explorations in this dynamic area of intrinsic magnetism and spin-based electronic devices.

4. Conclusions

In summary, the present work demonstrated the thickness-dependent properties of 2D $CoTe_2$. The theoretical and experimental observations conclude that the crystallographic orientations and structural changes are responsible for the mechanical behavior. The surface charge distribution changes as a function of number of layers. The obtained results for nanostructured $CoTe_2$ were compared with other 2D materials. The magnetic behavior changes as a function of layer number, which is due to the stacking order. We have demonstrated that the number of layers can be effectively used to tune and control some electronic and/or magnetic features, that can be helpful for designing next-generation tellurides-based devices.

Data availability statement

The data cannot be made publicly available upon publication because no suitable repository exists for hosting data in this field of study. The data that support the findings of this study are available upon reasonable request from the authors.

Acknowledgment

C.S.T. acknowledges Core research grant of SERB-India, STARS project by MHRD-India, DAE Young Scientist Research Award (DAEYSRA), and AOARD (Asian Office of Aerospace Research and Development) grant no. FA2386-23-14034. M.T. and A.B.D. would like to thank Sussex strategic development funds to carry out research at nanoscale.

Conflict of interest

The authors declare no competing financial/commercial conflicts of interest.

ORCID iDs

Manoj Tripathi https://orcid.org/0000-0002-8052-428X
Conor S Boland https://orcid.org/0000-0003-4376-6770
Alan Dalton https://orcid.org/0000-0001-8043-1377
Chandra Sekhar Tiwary https://orcid.org/0000-0001-9760-9768

References

[1] Chhowalla M, Shin H S, Eda G, Li L J, Loh K P and Zhang H 2013 The chemistry of two-dimensional layered transition metal dichalcogenide nanosheets *Nat. Chem.* **5** 263–75
[2] Tongay S, Zhou J, Ataca C, Lo K, Matthews T S, Li J, Grossman J C and Wu J 2012 Thermally driven crossover from indirect toward direct bandgap in 2D semiconductors: $MoSe_2$ versus MoS_2 *Nano Lett.* **12** 5576–80
[3] Lin Z *et al* 2016 2D materials advances: from large scale synthesis and controlled heterostructures to improved characterization techniques, defects and applications *2D Mater.* **3** 042001
[4] Mak K F and Shan J 2016 Photonics and optoelectronics of 2D semiconductor transition metal dichalcogenides *Nat. Photon.* **10** 216–26
[5] Zhou X, Hu X, Yu J, Liu S, Shu Z, Zhang Q, Li H, Ma Y, Xu H and Zhai T 2018 2D layered material-based van der Waals heterostructures for optoelectronics *Adv. Funct. Mater.* **28** 1706587
[6] Xiao Y, Li C, Tan X, Zhang L, Zhong Y and Zhu H 2017 Full-inorganic thin film solar cell and photodetector based on "Graphene-on-Antimony Sulfide" heterostructure *Solar RRL* **1** 1700135
[7] Cao T, Liu X, Cheng X, Li Y, Sang L, Ma J, Wang J, He J, Wang M and Zhang Y 2019 Unveiling the thickness-dependent mechanical properties of graphene papers by in situ SEM tension *RSC Adv.* **9** 4609–15
[8] Romanov R I, Kozodaev M G, Chernikova A G, Zabrosaev I V, Chouprik A A, Zarubin S S, Novikov S M, Volkov V S and Markeev A M 2021 Thickness-dependent structural and electrical properties of WS_2 nanosheets obtained via the ALD-grown WO_3 sulfurization technique as a channel material for field-effect transistors *ACS Omega* **6** 34429–37
[9] Wang H *et al* 2017 High-quality monolayer superconductor $NbSe_2$ grown by chemical vapour deposition *Nat. Commun.* **8** 1–8
[10] Lee C, Li Q, Kalb W, Liu X Z, Berger H, Carpick R W and Hone J 2010 Frictional characteristics of atomically thin sheets *Science* **328** 76–80
[11] Lebègue S, Björkman T, Klintenberg M, Nieminen R M and Eriksson O 2013 Two-dimensional materials from data filtering and ab initio calculations *Phys. Rev.* X **3** 031002
[12] Li J *et al* 2018 Synthesis of ultrathin metallic MTe_2 (M = V, Nb, Ta) single-crystalline nanoplates *Adv. Mater.* **30** 1801043
[13] Zhou S, Wang R, Han J, Wang D, Li H, Gan L and Zhai T 2019 Ultrathin non-van der Waals magnetic rhombohedral Cr_2S_3: space-confined chemical vapor deposition synthesis and Raman scattering investigation *Adv. Funct. Mater.* **29** 1805880
[14] Wang H, Wang Y, Tan L, Fang L, Yang X, Huang Z, Li J, Zhang H and Wang Y 2019 Component-controllable cobalt telluride nanoparticles encapsulated in nitrogen-doped carbon frameworks for efficient hydrogen evolution in alkaline conditions *Appl. Catal.* B **244** 568–75
[15] Liu Z, Tao Y, Cui Z, Ji Y, Zhou X, Li P, Zhang Y and Zhong D 2023 A two-dimensional tetragonal structure of vanadium telluride *Nano Res.* **16** 7749–55
[16] Fang H, Luo Z, Yang H and Wu Y 2014 The effects of the size and the doping concentration on the power factor of n-type lead telluride nanocrystals for thermoelectric energy conversion *Nano Lett.* **14** 1153–7
[17] Rosati R, Brem S, Perea-Causín R, Schmidt R, Niehues I, de Vasconcellos S M, Bratschitsch R and Malic E 2020 Strain-dependent exciton diffusion in transition metal dichalcogenides *2D Mater.* **8** 015030
[18] Muhler M, Bensch W and Schur M 1998 Preparation, crystal structures, experimental and theoretical electronic band structures of cobalt tellurides in the composition range *J. Phys.: Condens. Matter* **10** 2947
[19] Ma H *et al* 2018 Chemical vapor deposition growth of single crystalline $CoTe_2$ nanosheets with tunable thickness and electronic properties *Chem. Mater.* **30** 8891–6
[20] Wang X *et al* 2020 Thickness-controlled synthesis of CoX_2 (X = S, Se, and Te) single crystalline 2D layers with linear magnetoresistance and high conductivity *Chem. Mater.* **32** 2321–9
[21] Negedu S D *et al* 2022 Two-dimensional cobalt telluride as a piezo-tribogenerator *Nanoscale* **14** 7788–97
[22] Zhang H, Huang J, Wang Y, Liu R, Huai X, Jiang J and Anfuso C 2018 Atomic force microscopy for two-dimensional materials: a tutorial review *Opt. Commun.* **406** 3–17
[23] Clark N, Oikonomou A and Vijayaraghavan A 2013 Ultrafast quantitative nanomechanical mapping of suspended graphene *Phys. Status Solidi* B **250** 2672–7
[24] Tripathi M *et al* 2021 Structural defects modulate electronic and nanomechanical properties of 2D materials *ACS Nano* **15** 2520–31
[25] Susarla S, Manimunda P, Morais Jaques Y, Hachtel J A, Idrobo J C, Syed Amnulla S A, Galvão D S, Tiwary C S and Ajayan P M 2018 Deformation mechanisms of vertically stacked WS_2/MoS_2 heterostructures: the role of interfaces *ACS Nano* **12** 4036–44
[26] Tripathi M *et al* 2022 Probing the interaction between 2D materials and oligoglycine tectomers *2D Mater.* **9** 045033
[27] Li Z *et al* 2020 Mechanisms of liquid-phase exfoliation for the production of graphene *ACS Nano* **14** 10976–85
[28] Sader J E, Pacifico J, Green C P and Mulvaney P 2005 General scaling law for stiffness measurement of small

bodies with applications to the atomic force microscope *J. Appl. Phys.* **97** 124903
[29] Ceperley D M and Alder B J 1980 Ground state of the electron gas by a stochastic method *Phys. Rev. Lett.* **45** 566
[30] Soler J M, Artacho E, Gale J D, García A, Junquera J, Ordejón P and Sánchez-Portal D 2002 The SIESTA method for ab initio order-N materials simulation *J. Phys.: Condens. Matter* **14** 2745
[31] Li J, Yang Y, Li L, Lou J, Luo X and Huang B 2013 Interfacial properties and electronic structure of β-SiC (111)/α-Ti (0001): a first principle study *J. Appl. Phys.* **113** 023516
[32] Khatun S, Banerjee A and Pal A J 2019 Nonlayered tellurene as an elemental 2D topological insulator: experimental evidence from scanning tunneling spectroscopy *Nanoscale* **11** 3591–8
[33] Du Y, Qiu G, Wang Y, Si M, Xu X, Wu W and Ye P D 2017 One-dimensional van der Waals material tellurium: Raman spectroscopy under strain and magneto-transport *Nano Lett.* **17** 3965–73
[34] Kalampounias A G, Yannopoulos S N and Papatheodorou G N 2017 Vibrational modes of sodium–tellurite glasses: local structure and Boson peak changes *J. Phys. Chem. Solids* **68** 1035–9
[35] Wang X, Huang X, Gao W, Tang Y, Jiang P, Lan K, Yang R, Wang B and Li R 2018 Metal–organic framework derived $CoTe_2$ encapsulated in nitrogen-doped carbon nanotube frameworks: a high-efficiency bifunctional electrocatalyst for overall water splitting *J. Mater. Chem.* A **6** 3684–91
[36] Biesinger M C, Payne B P, Grosvenor A P, Lau L W, Gerson A R and Smart R S 2011 Resolving surface chemical states in XPS analysis of first row transition metals, oxides and hydroxides: Cr, Mn, Fe, Co and Ni *Appl. Surf. Sci.* **257** 2717–30
[37] Tripathi M, King A, Fratta G, Meloni M, Large M, Salvage J P, Pugno N M and Dalton A B 2018 Laser-based texturing of graphene to locally tune electrical potential and surface chemistry *ACS Omega* **3** 17000–9
[38] Derjaguin B V, Muller V M and Toporov Y P 1975 Effect of contact deformations on the adhesion of particles *J. Colloid Interface Sci.* **53** 314–26
[39] Offroy M, Razafitianamaharavo A, Beaussart A, Pagnout C and Duval J F 2020 Fast automated processing of AFM PeakForce curves to evaluate spatially resolved Young modulus and stiffness of turgescent cells *RSC Adv.* **10** 19258–75
[40] Lee J U, Yoon D and Cheong H 2012 Estimation of Young's modulus of graphene by Raman spectroscopy *Nano Lett.* **12** 4444–8
[41] Falin A *et al* 2017 Mechanical properties of atomically thin boron nitride and the role of interlayer interactions *Nat. Commun.* **8** 15815
[42] Bertolazzi S, Brivio J and Kis A 2011 Stretching and breaking of ultrathin MoS_2 *ACS Nano* **5** 9703–9
[43] Filleter T, McChesney J L, Bostwick A, Rotenberg E, Emtsev K V, Seyller T, Horn K and Bennewitz R 2009 Friction and dissipation in epitaxial graphene films *Phys. Rev. Lett.* **102** 086102
[44] Ye Z, Balkanci A, Martini A and Baykara M Z 2017 Effect of roughness on the layer-dependent friction of few-layer graphene *Phys. Rev.* B **96** 115401
[45] Egberts P, Han G H, Liu X Z, Johnson A C and Carpick R W 2014 Frictional behavior of atomically thin sheets: hexagonal-shaped graphene islands grown on copper by chemical vapor deposition *ACS Nano* **8** 5010–21
[46] Fang L, Liu D M, Guo Y, Liao Z M, Luo J B and Wen S Z 2017 Thickness dependent friction on few-layer MoS_2, WS_2, and WSe_2 *Nanotechnology* **28** 245703
[47] Zhang Q, Ma X and Zhao Y 2018 Adhesion behavior between multilayer graphene and semiconductor substrates *Appl. Sci.* **8** 2107
[48] Yoon T, Shin W C, Kim T Y, Mun J H, Kim T S and Cho B J 2012 Direct measurement of adhesion energy of monolayer graphene as-grown on copper and its application to renewable transfer process *Nano Lett.* **12** 1448–52
[49] Deng S, Gao E, Xu Z and Berry V 2017 Adhesion energy of MoS_2 thin films on silicon-based substrates determined via the attributes of a single MoS_2 wrinkle *ACS Appl. Mater. Interfaces* **9** 7812–8
[50] Li Y, Huang S, Wei C, Wu C and Mochalin V N 2019 Adhesion of two-dimensional titanium carbides (MXenes) and graphene to silicon *Nat. Commun.* **10** 3014
[51] Choi S, Shaolin Z and Yang W 2014 Layer-number-dependent work function of MoS_2 nanoflakes *J. Korean Phys. Soc.* **64** 1550–5
[52] Kim H G and Choi H J 2021 Thickness dependence of work function, ionization energy, and electron affinity of Mo and W dichalcogenides from DFT and GW calculations *Phys. Rev.* B **103** 085404
[53] Dai Z, Lu N, Liechti K M and Huang R 2020 Mechanics at the interfaces of 2D materials: challenges and opportunities *Curr. Opin. Solid State Mater. Sci.* **24** 100837
[54] Marchiori E, Ceccarelli L, Rossi N, Lorenzelli L, Degen C L and Poggio M 2022 Nanoscale magnetic field imaging for 2D materials *Nat. Rev. Phys.* **4** 49–60
[55] Li H, Qi X, Wu J, Zeng Z, Wei J and Zhang H 2013 Investigation of MoS_2 and graphene nanosheets by magnetic force microscopy *ACS Nano* **7** 2842–9
[56] Jaafar M, Iglesias-Freire O, Serrano-Ramón L, Ibarra M R, de Teresa J M and Asenjo A 2011 Distinguishing magnetic and electrostatic interactions by a Kelvin probe force microscopy–magnetic force microscopy combination *Beilstein J. Nanotechnol.* **2** 552–60
[57] Li T *et al* 2019 Pressure-controlled interlayer magnetism in atomically thin CrI_3 *Nat. Mater.* **18** 1303–8
[58] Zhang S, Xu R, Luo N and Zou X 2021 Two-dimensional magnetic materials: structures, properties and external controls *Nanoscale* **13** 1398–424
[59] Huang Y L, Chen W and Wee A T 2021 Two-dimensional magnetic transition metal chalcogenides *SmartMat* **2** 139–53
[60] Siegfried P E *et al* 2023 $CoTe_2$: a quantum critical Dirac metal with strong spin fluctuations *Adv. Mater.* **35** 2300640